Chemical Engineering Journal 493 (2024) 152492

Contents lists available at ScienceDirect

Chemical Engineering Journal

journal homepage: www.elsevier.com/locate/cej

The dual-band emission with long-lived thermally activated delayed fluorescence and room temperature phosphorescence by trace ingredient incorporation

Lijuan Shi [a,1], Jiaqi Liu [b,1], Lei Ma [b,*], Yongtao Wang [a,*]

[a] Guangxi Key Laboratory of Electrochemical and Magneto-chemical Function Materia, College of Chemistry and Bioengineering, Guilin University of Technology, Guilin 541004, China
[b] Tianjin International Center for Nanoparticles and Nanosystem, Tianjin University, Tianjin, 300072, China

ARTICLE INFO

Keywords:
Room temperature phosphorescence
Thermally activated delayed fluorescence
Host-guest doping
Long-Lived phosphorescence
Dual-band emission

ABSTRACT

The dual band purely organic room temperature phosphorescent (p-ORTP) materials with persistent thermally activated delayed fluorescence (TADF) and room-temperature phosphorescence (RTP) can achieve time dependent afterglow and unique afterglow response under heating and mechanical force, show very important values on theoretical and practical application. Here, 2-benzylmalononitrile derivatives and a series of impurities were characterized and confirmed by NMR, HR-MS, and single-crystal X-ray diffraction, forming host–guest bicomponent systems with dual-band and long-lived TADF (410 nm) and RTP (490–510 nm). At room temperature, TADF and RTP lifetimes are up to 1056 ms and 1027 ms in sequence. The intensity ratio between TADF and RTP can be well adjusted by grinding, temperature, as well as host and guest materials, presenting color-tunable and time-dependent afterglow from green to blue. Owing to the excellent crystallinity, the bicomponent systems also display lower sensitivity to external environments such as water vapor and oxygen. The high-level digital and program encryption, and anti-counterfeiting patterns were successfully constructed based on temperature sensitivity, and different TADF and RTP afterglow lifetimes of the doping systems. The work also provides deep blue persistent glow and clears the obstacles for large-scale production. Most importantly, this work will provide a novel and efficient method for the development of dual band and long-lived TADF and RTP materials.

1. Introduction

Purely organic room temperature phosphorescent (p-ORTP) materials can overcome the drawbacks of traditional inorganic phosphorescent materials such as high cost, biological toxicity, and environmental pollution, and show better flexibility, color tunability, and transparency [1–6]. Recently, p-ORTP materials show tremendous potential for constructing high-level information encryption [7–9], advanced optoelectronic devices [10,11], and biosensing and imaging without background interference [12–14]. However, p-ORTP materials suffer from ineffective intersystem crossing (ISC) between singlet and triplet and rapid nonradiative transition, causing scarcity of p-ORTP materials with high efficiency (> 10 %) and long lifetime (> 100 ms)[15]. Based on crystal engineering and host–guest doping, the above issues have been effectively alleviated [16–19]. However, there are still very few p-ORTP materials with phosphorescence lifetime exceeding 1000 ms. Furthermore, triplet excitons are sensitive to external environments such as oxygen, water vapor, and mechanical forces, and thereby most of p-ORTP materials experience rapid attenuation or quenching of triplet excitons in aqueous solution or after grinding, while some p-ORTP materials generate bright afterglows requiring 20–60 s UV irradiation for deoxygenation [17,20,21]. Currently, constructing efficient and stable p-ORTP materials still faces significant challenges by more reliable mechanism and convenient strategies. Most importantly, the introduction of dual band persistent luminescent species with thermally activated delayed fluorescence (TADF) and room-temperature phosphorescence (RTP) can achieve time dependent afterglow and unique afterglow response under heating and mechanical force by adjusting the

* Corresponding authors.
E-mail addresses: lei.ma@tju.edu.cn (L. Ma), wyt_shzu@163.com (Y. Wang).
[1] Contributed equally.

https://doi.org/10.1016/j.cej.2024.152492
Received 11 April 2024; Received in revised form 20 May 2024; Accepted 22 May 2024
Available online 23 May 2024

components of TADF and RTP, and thereby significantly enhance the difficulty of forgery [22–26]. However, the lifetime of TADF type p-ORTP materials rarely exceeds 1000 ms, not to mention dual band p-ORTP materials with persistent TADF and RTP [27–30].

Notably, many luminogens based on commercial carbazole as starting materials showed bright ultralong organic room-temperature phosphorescence (UORTP), but the same compounds derived from laboratory synthesized carbazole usually provide poor RTP lifetimes and quantum yields, even imperceptible RTP to the naked eyes [31–33]. Furthermore, the trace impurities Bd (1H-benzo[f]indole) are still difficult to completely eliminate by column chromatography, recrystallization, and even sublimation [34,35]. Thereby, the impact of trace impurities on RTP performance has attracted widespread attention of researchers during the synthesis process [36,37]. Recently, some Bd derivatives were prepared and used as guest materials by Ma and his group [38,39], and the mechanism and influencing factors of charge separation states were further explored in detail. However, preparation of Bd needs strict reaction conditions and long synthesis steps, which combined with a low yield limit its wide applications in p-ORTP materials and doping systems. Therefore, the exploration of new and feasible alternatives imitating the function of Bd is significance and full of challenges. Unfortunately, few impurity research was reported in the p-ORTP systems [38,39].

By one pot multi-step reactions under the catalysis of triethylamine (Scheme S1), 2-benzylmalononitrile and its halogenated derivatives named as TCN-H, TCN-F, TCN-Cl and TCN-Br were designed and synthesized, emitting green or blue persistent RTP. Different synthesis routes and careful separation and purification indicate a series of trace impurities are essential to generate RTP. Then, a series of trace impurities were characterized and confirmed to be 3-amino-[1,1′-biphenyl]-2,4-dicarbonitrile (BTDA-H) and its halogenated derivatives (BTDA-F, BTDA-Cl and BTDA-Br). Further research confirmed phosphorescent nature of BTDA series luminogens, but not for TCN series luminogens themselves. TCN and BTDA series luminogens were used as host and guest materials in sequence, whose doping systems were established and optimized by melt blending and adjusting the doping mass ratios of host and guest materials from 10000:1 to 10:1. Taking 1 % TCN-H/BTDA-H and 1 % BTDA-H@PMMA film as examples, BTDA-H was doped separately in TCN-H and PMMA at the mass ratio of 1:100 in turn. According to this rule, other doping systems were named. Among of the doping systems, the maximum RTP lifetime is up to 1027 ms simultaneously with RTP quantum yield of 0.107 for the pure organic 1 % TCN-H/BTDA-H doping system. More amazing, 1 % TCN-H/BTDA-H also presents a strong TADF peak at room temperature (RT), with TADF lifetimes of 1056 ms. Taking 1 % TCN-H/BTDA-H as an example, the influences of host and guest materials on RTP and TADF were investigated in detail by choosing different host and guest materials, confirming the superiority of TCN-H, stability of TADF emission maxima, and adjustability of intensity ratio (I_{TADF}/I_{RTP}) between TADF and RTP. Subsequently, a new 1 % TCN-H/BTDA-Me doping system were constructed based on similar molecular structure between BTDA-Me and BTDA-H, as well as a more efficient synthesis method, also generating efficient TADF and RTP. It is worth noting that the synthesis of TCN-H and BTDA-Me can be easily expanded to the kilogram level due to short synthesis steps, mild reaction conditions (RT), and high yield (>80 %). More importantly, the doping systems display lower sensitivity to external environments such as water vapor, oxygen, and mechanical forces, indicating dynamic persistent afterglow after grinding. When four guests were doped in polymethyl methacrylate (PMMA) at the weight ratio of 1:100, the doping films also showed dual band persistent TADF and RTP emission, with high sensitivity to surrounding temperatures due to reverse responsive TADF and RTP. Finally, high-level digital and program encryption, and anti-counterfeiting patterns were successfully constructed based on temperature sensitivity, and different TADF and RTP afterglow lifetimes of the doping systems. Based on trace impurity research, this work provides a series of new host–guest doping systems, with rare dual-band persistent TADF and RTP emission. Moreover, BTDA-Me shows scare deep-blue afterglow in PMMA film. By designing dual state long afterglow materials, and further adjusting TADF and RTP luminescent modes, this work contributes to solve the problems of homogenization and singularity in long afterglow materials. More importantly, this work not only provides a solid theoretical foundation for dual state long afterglow materials, but also supports for the development of high-level anti-counterfeiting and digital encryption.

2. Results and discussion

2.1. Impurity in RTP organism

As shown in Scheme 1 and Scheme S1-S3, TCN-H, TCN-F, TCN-Cl and TCN-Br were synthesized via a one-step reaction and purified by column chromatography and recrystallization. Switching-on/off 365 nm UV lamp, the four luminogens emit persistent green RTP with afterglow of 0.5–4 s (Fig. 1b). What is more, RTP spectra of the four luminogens have the following two characteristics:(1) crystal TCN-H shows dual-band delayed emission at 410 nm and 500 nm, but inconspicuous for the other three luminogens at 410 nm; (2) phosphorescence maxima of crystal TCN-Br display an obvious red shift compared with the other three luminogens due to a larger atomic radius for Br than Cl, F, and H (Fig. 1c). Furthermore, a new synthesis route was selected by condensation and reduction reactions under the catalysis of K_2CO_3 and $BH_3{\cdot}NH_3$ (Scheme 2) due to poor reaction yields for Scheme 1. As expected, the luminogens were obtained with high yields, and their structures were further analyzed and characterized by TLC, NMR, HR-MS, and X ray single crystal diffraction. Comparison of afterglows indicated that the RTP of TCN series luminogens come from the trace impurities. To ascertain molecular structures of the impurities, a large number of TCN-H TCN-F, TCN-Cl and TCN-Br were synthesized by Scheme 1. Fortunately, the impurities named as BTDA-H, BTDA-F, BTDA-Cl and BTDA-Br were successfully separated and purified by flash column chromatography and high-performance liquid chromatography (Fig. S27, Fig. S28), whose structures were characterized by ^{1}H NMR, ^{13}C NMR and HR-MS (Fig. S13-S24). By slow solvent diffusion from n-hexane to DCM solution of BTDA-Cl, a colorless needle-like crystal was obtained, presenting blue fluorescence under radiation of 365 nm, whose structure was further confirmed by single crystal diffraction. Furthermore, no afterglow can be observed by switching on/off UV lamp at room temperature, and the same phenomenon also occurs on crystals BTDA-H, BTDA-F and BTDA-Br. When DCM solution of BTDA series luminogens were cooled to 77 K, bright green afterglows were observed by switching on/off UV lamp, confirming phosphorescent nature of the luminogens (Fig. 2a). Moreover, phosphorescence spectra continue to red shift with the the increasing atomic number from H, F, Cl to Br, indicating that halogen atoms can affect triplet state energy levels of the luminogens. Subsequently, phosphorescence performance of TCN series luminogens were also investigated in DCM solution at 77 K, but no afterglow could be perceived. In view of the above situation, we reached the following preliminary conclusions: 1) a series of novel bicomponent RTP systems can be constructed by one pot multi-step reactions; 2) TCN and BTDA series luminogens serve as host and guest materials respectively in bicomponent RTP systems, and the two series luminogens have excellent compatibility; 3) Halogen atoms are not conducive to persistent RTP and dual-band delayed emission of the bicomponent systems, and the pure organic TCN-H/BTDA-H system shows the longest afterglow lifetime among of the bicomponent RTP systems, without a definite doping ratio.

2.2. Photophysical properties in solution.

When trace guests are uniformly dispersed in hosts, guests exist in the form of monomer, and thereby show guest monomer phosphorescence. In host–guest doping systems, host materials are not limited to

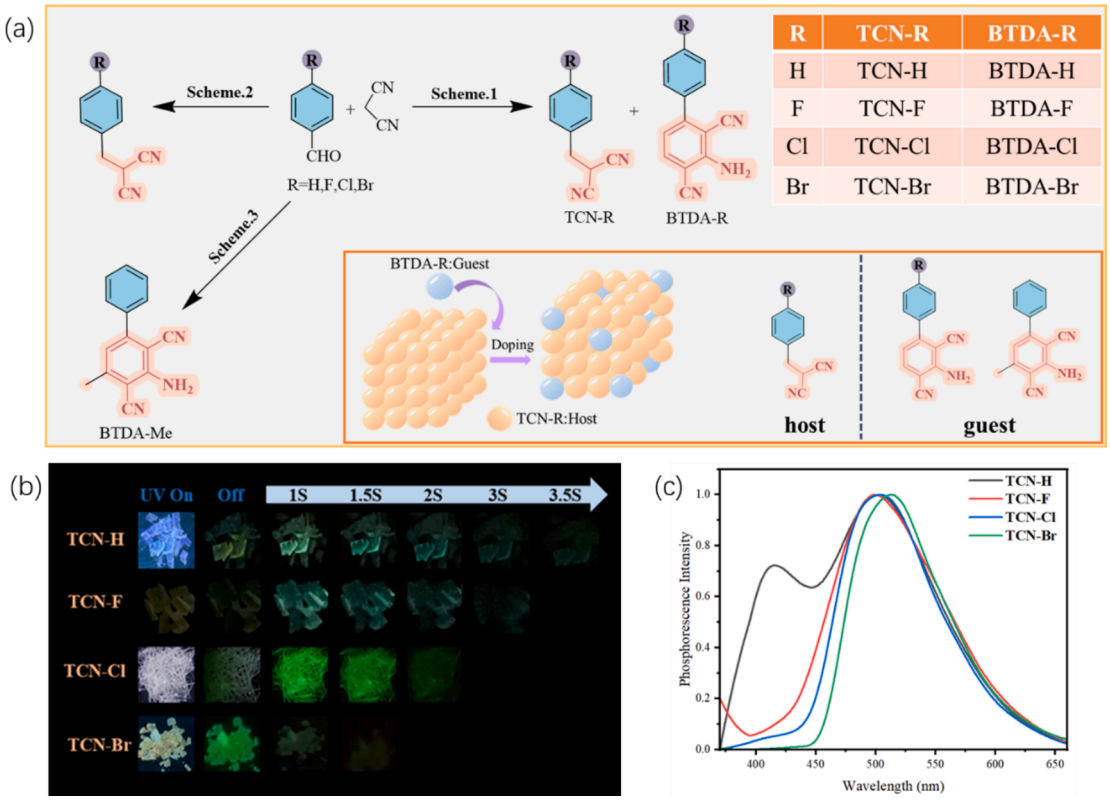

Fig. 1. (a) Synthesis routes of the two series luminogens (Scheme S1-S3.); (b) Digital photographs of TCN series luminogens containing trace BTDA derivatives by the on–off switching of 365 nm UV lamp; (c) Delayed RTP spectra of TCN series luminogens containing trace BTDA derivatives (delayed time τ_d: 1 ms, λ_{ex}: 365 nm);.

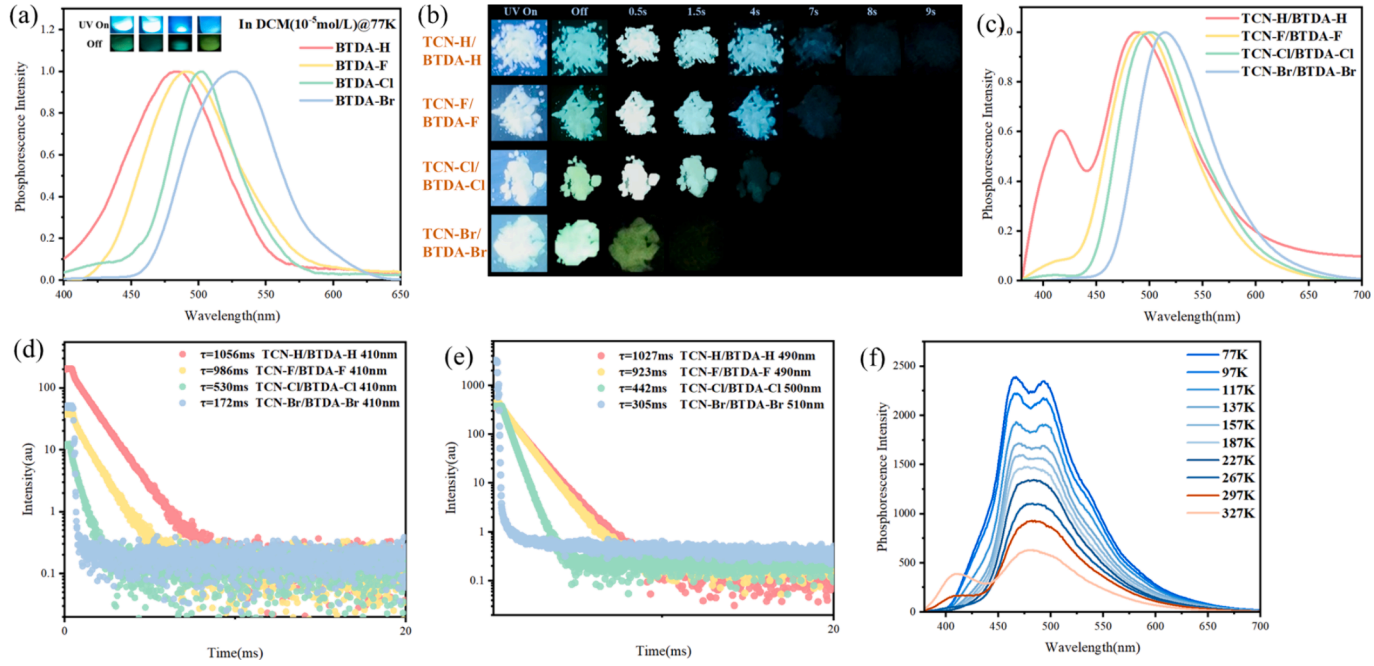

Fig. 2. (a) Delayed spectra of BTDA-H, BTDA-F, BTDA-Cl, and BTDA-Br in DCM solution at low temperatures (77 K); (b) Digital photographs of 1 % TCN-H/BTDA-H, 1 % TCN-F/BTDA-F, 1 % TCN-Cl/BTDA-Cl and 0.01 % TCN-Br/BTDA-Br by the on–off switching of 365 nm UV lamp; (c) Delayed spectra of1% TCN-H/BTDA-H, 1 % TCN-F/BTDA-F, 1 % TCN-Cl/BTDA-Cl and 0.01 % TCN-Br/BTDA-Br at room temperature (τ_d = 1 ms, λ_{ex}: 365 nm); (d) TADF (e) and RTP decay curves of 1 % TCN-H/BTDA-H, 1 % TCN-F/BTDA-F, 1 % TCN-Cl/BTDA-Cl and 0.01 % TCN-Br/BTDA-Br; (f) Temperature-variable phosphorescence spectra of 1 % TCN-H/BTDA-H.

restrict non-radiative decay of triplet excitons, they also serve as an energy bridge between the singlet and triplet states between guests [35,40–42]. Besides, BTDA series derivatives are new fluorescent chromophores, whose photophysical properties have not been reported yet. To reveal the mechanism behind phosphorescence and clarify the photophysical properties of BTDA series luminogens, photophysical

properties of TCN and BTDA derivatives were firstly investigated in solution. Fig S27 shows that TCN derivatives have two absorption bands at 230 and 265 nm in DCM solution (10 μM), corresponding to E2 and B-band absorption of substituted benzene ring respectively. Interestingly, all four TCN derivatives present two fluorescence emission bands around 400 nm and 500 nm (Fig S28) when excited at absorption maxima (265 nm), and two fluorescence emission bands with different excitation spectra (Fig S29). Moreover, excitation dependent emission spectra were also observed, which show different intensity ratios between two fluorescence emission bands under excitation of 230 nm, 265 nm, and 275 nm, but with stable emission peaks. As we know, quinine sulfate may have multiple molecular conformations at different excitation wavelengths, and the energy levels of these conformations vary, resulting in dual-band fluorescence emissions at different excitation wavelengths. Thereby, dual band and excitation dependent emission spectra of the TCN derivatives may be attributed to different molecular conformations. Significantly, Stokes shifts of TCN derivatives are up to 280 nm, which may be due to the strong molecular relaxation induced by sp^3-methylene linkers in solution. To obtain a secondhand evidence, emission spectra of TCN derivatives were investigated in crystalline state, whose emission maxima show significant blue shifts compared with that in solution due to twisted molecular conformation and strong intermolecular interactions (Fig S30). In DCM solution (10 μM, Fig S31), BTDA derivatives have four absorption bands from 225 nm to 380 nm, whose fluorescence emission spectra almost completely overlap between BTDA-H and BTDA-F, but with bathochromic-shifts of 25 nm for BTDA-Cl and BTDA-Br than BTDA-H and BTDA-F, indicating fluorescence emission maxima are related to the radius of halogen atoms. By selecting THF and H_2O as benign and non-benign solvents (Fig S32-33), aggregation-induced emission (AIE) activity of BTDA derivatives were measured. Overall, BTDA derivatives show aggregation-induced enhanced emission (AIEE) activity, emitting strong blue fluorescence in THF-H_2O solution, while significant decrease in emission intensity for BTDA-Cl and BTDA-Br is due to the precipitation of two luminogens at water fraction of 90 %. When DCM solutions of the luminogens are spotted on the thin layer silicone plate (TLC, Fig S34), the above phenomenon can be revealed by directly observing under ultraviolet light. With the continuous volatilization of DCM, BTDA-H always emits strong violet fluorescence. Furthermore, the relative fluorescence quantum yields (PLQYs) of the luminogens were determined in DCM by using quinine sulfate as a reference, with PLQYs of 0.57, 0.49, 0.40 and 0.34 for BTDA-H, BTDA-F, BTDA-Cl and BTDA-Br in turn (Table S1), which should be attributed to the enhanced spin-orbital coupling (SOC), leading to the reduced PLQYs. As a summary of this paragraph, the BTDA derivatives show dual-band fluorescence emissions, with bright fluorescence in solution and solid state, but the introduction of halogen atoms, especially heavy atom (Br), plays a negative role in the fluorescence emission, leading to lower PLQYs for BTDA-F, BTDA-Cl and BTDA-Br than BTDA-H in DCM solution.

2.3. Design of trace ingredient-mediated bicomponent RTP systems

The impurities BTDA-H, BTDA-F, BTDA-Cl and BTDA-Br were discovered by chance, but it was common for RTP induced by trace impurity. As documented, TCN and BTDA series luminogens function as host and guest materials, respectively. Furthermore, the bicomponent RTP systems can be optimized and redesigned by adjusting the doping ratio and combination mode between host and guest materials. Based on the lower melting point for the host materials (85–110 ℃), BTDA series luminogens were doped into the corresponding TCN derivatives by melting method, with doping ratios from 10:1 to 10000:1. The persistent afterglows display (Fig. S35-38) that the optimal doping ratio of TCN-H/BTDA-H, TCN-F/BTDA-F and TCN-Cl/BTDA-Cl is 100:1, but 10000:1 for TCN-Br/BTDA-Br doping system possibly due to heavy-atom effect, which boost ISC and the resulting collision quenching between triplet excitons at high concentrations. Amazing, afterglow lifetime of 1 % TCN-H/BTDA-H doping system lasts for 9 s, but it continues to decrease with the introduction of halogen atoms and the increase of atomic number (Fig. 2b). Different from green afterglow of BTDA derivatives in DCM solution at 77 K, 1 % TCN-H/BTDA-H bicomponent system presents blue afterglow due to the emergence of a new and strong delay peak at 410 nm. The delayed phosphorescence spectra of four doping systems show dual-band emission at 410 nm and 490–510 nm, but the intensity ratio between 410 nm and 490–510 nm decreases sequentially from 1 % TCN-H/BTDA-H, 1 % TCN-F/BTDA-F, 1 % TCN-Cl/BTDA-Cl to 0.01 % TCN-Br/BTDA-Br, which is consistent with the observed afterglow color from blue to green (Fig. 2c). The emission maxima of the four guests also show continuous redshifts from BTDA-H, BTDA-F, BTDA-Cl to BTDA-Br, which are consistent with the emission in DCM solution at 77 K, further demonstrating that the introduction of halogen atoms can reduce the triplet state energy level of BTDA-H. More amazingly, the emission maxima at 410 nm and 490–510 nm show ultralong delay lifetimes with 172–1056 ms at RT, confirming their RTP or TADF characteristic (Fig. 2d-2e). Owing to equivalent delay lifetimes between 410 nm and 490–510 nm, triplet–triplet annihilation mechanism is eliminated. To further investigate characteristics of the two long-lived emission peaks, temperature-variable phosphorescence spectra of 1 % TCN-H/BTDA-H were performed (Fig. 2f). 1 % TCN-H/BTDA-H presents two emission peaks from 77 K to 157 K, located at 470 nm and 490 nm respectively, which is attributed to fine vibration of the emission band. Subsequently, a single emission peak at 480 nm can be observed, accompanied by a continuous decrease in emission intensity. Of note, the emission peak at 410 nm begins to appear when the temperature rises to 297 K, and significantly enhances with the temperature further increases to 327 K. Thereby, the emission peaks of 1 % TCN-H/BTDA-H at 410 nm and 490 nm belong to TADF and RTP in turn. Furthermore, the energy gaps (ΔE_{ST}) of the four doped systems between the lowest singlet(S_1) and lowest triplet (T_1) states were calculated based on the above spectral test results (Table 1). The absolute TADF and RTP quantum yields of four doping systems were measured by the integrating sphere in crystalline state, and the corresponding data were listed in Table 1. By contrast, the introduction of halogen atoms and increasing atom radius shorten TADF and RTP lifetimes, reduce the TADF quantum yield (Φ_{TADF}), but improve the RTP quantum yield (Φ_P). Li et al[39] found the host with bromide ions results in the absence of TADF emission in the dual-state afterglow systems, which is ascribed to the heavy-atom effect of bromide ions, enhancing SOC and ISC. Thereby, the reduced Φ_{TADF} and the enhanced Φ_P should be due to the gradually enhanced SOC and ISC for the four host–guest doping systems. Notably, TADF and RTP lifetimes of 1 % TCN-H/BTDA-H are up to 1056 ms and 1027 ms in turn, which is rare for a pure organic doping system simultaneously possesses such long-lived RTP and TADF (Table.1). To elucidate RTP mechanism of the above doping systems, fluorescence spectra of TCN and BTDA series luminogens, as well as absorption spectra of BTDA series luminogens were recorded in crystalline state (Fig. S39-40). The results indicate that emission maxima of crystals BTDA-H, BTDA-F and BTDA-Br are located at 438 nm, but emission maxima of crystal BTDA-Cl redshifts to 455 nm probably due to different intermolecular arrangements and stacking modes. By comparison, RTP maxima of four doping systems around 500 nm approach that of guest monomers in DCM at 77 K, which belong to the intrinsic phosphorescence of guests. Meanwhile, we also ruled out the possibility that TADF emission of the doping systems comes from host materials due to the obvious discrepancy between TADF emission maxima and crystalline fluorescence emission of host materials. Notably, the TADF emission maxima are very close to fluorescence emission maxima of the guests in DCM solution rather than crystalline state. Therefore, The TADF emission of the doping systems may come from the guest monomer. Besides, crystalline fluorescence emission spectra of TCN derivatives overlap with absorption spectra of BTDA derivatives in solution very well (Fig. S40), illustrating effective FÖster resonance energy transfer can occur from the hosts to the guests in the doping systems. Furthermore, taking TCN-H/BTDA-H as an

Table 1
Photophysical properties of 1% TCN-H/BTDA-H, 1% TCN-F/BTDA-F, 1% TCN-Cl/BTDA-Cl and 0.01% TCN-Br/BTDA-Br.

	λ_{TADF} [nm]	λ_p [nm]	τ_{TADF} [ms]	τ_p [ms]	Φ_{TADF} [%]	Φ_P [%]	K_{ISC} [s^{-1}]	K_p [s^{-1}]	K_{nr} [s^{-1}]	ΔE_{ST} [eV]
TCN-H/BTDA-H	410	490	1056	1027	2.6	10.7	4.6x10^8	0.15	0.82	0.49
TCN-F/BTDA-F	410	495	986	923	0.27	10.03	2.7 x10^8	0.14	0.94	0.51
TCN-Cl/BTDA-Cl	410	500	531	442	0.14	14.86	4.6 x10^8	0.42	1.84	0.54
TCN-Br/BTDA-Br	410	510	–	305	–	24.1	3.2 x10^8	1.05	2.23	0.59

example, UV–Vis absorption spectra of TCN-H, BTDA-H, TCN-H/BTDA-H were investigated in solid state (Fig S41). Owing to the absence of a new absorption peak, exciplex is excluded. At different excitation wavelengths, 1 % TCN-H/BTDA-H presents the strongest RTP emission under 365 nm excitation, followed by 280 nm and 430 nm. Given absorption spectra of TCN-H, BTDA-H, and TCN-H/BTDA-H, RTP mechanism of 1 % TCN-H/BTDA-H should mainly be coexcitation of guest and host, energy transfer from host to guest, and host sensitized RTP.

The influences of hosts on RTP and TADF emission of the doping systems were further investigated by constructing new doping systems, which were called as 1 % TCN-F/BTDA-H, 1 % TCN-Cl/BTDA-H, and 1 % TCN-Br/BTDA-H. The results show that 1 % TCN-H/BTDA-H is still better doping system compared with the other new doping systems, whose afterglows are shortened to 8 s, 8 s and 3 s from 9 s, corresponding to RTP (TADF) lifetimes of 921 ms (788 ms), 772 ms (625 ms), and 310 ms (381 ms) in sequence. Notably, RTP and TADF lifetimes of 1 % TCN-Cl/BTDA-Cl and 1 % TCN-Br/BTDA-Br are shorter than the corresponding 1 % TCN-Cl/BTDA-H and 1 % TCN-Br/BTDA-H due to the heavy atom effect of guests, but longer for 1 % TCN-F/BTDA-F than 1 % TCN-F/BTDA-H, which should be ascribed to better compatibility for the former than the latter. More importantly, TADF and RTP emission maxima of the doping systems maintain constant with the changing of hosts, whereas I_{TADF}/I_{RTP} is significantly reduced from 1 % TCN-H/BTDA-H to 1 % TCN-F/BTDA-H, 1 % TCN-Cl/BTDA-H, and 1 % TCN-Br/BTDA-H. Moreover, I_{TADF}/I_{RTP} of 1 % TCN-Cl/BTDA-H and 1 % TCN-Br/BTDA-H also show slight increase compared with 1 % TCN-Cl/BTDA-Cl and 1 % TCN-Br/BTDA-Br, further indicating the hosts and guests with strong SOC facilitate RTP emission of the doping systems, but not for TADF emission. The reported literature[39] indicated that I_{TADF}/I_{RTP} is negatively correlated with energy differences (ΔE_{T1T1}) between T_1 states of host and guest. In other words, I_{TADF}/I_{RTP} gradually increases as the ΔE_{T1T1} decreases. Therefore, energy levels of T_1 state were calculated for TCN-H (2.81 eV), TCN-F (2.77 eV), TCN-Cl (2.46 eV), TCN-Br (2.39 eV) and BTDA-H (2.06 eV), indicating continuous decline of ΔE_{T1T1} from TCN-H (0.75 eV), TCN-F (2.71 eV), TCN-Cl (0.40 eV) to TCN-Br (0.33 eV). Obviously, the calculation results are inconsistent with the the above conclusion. Furthermore, the main energy levels and spin orbit coupling constants (ξ) of BTDA-H show that there are two triplet states (T_3 and T_4) above the S_1 state and two triplet states (T_1 and T_2) below the S_1 state, but it is difficult to generate effective ISC and reversible intersystem transition (RISC) between S_1 and T_1 due to tiny ξ (0.095 cm^{-1}) and large energy gap (1.25 eV). Owing to the large energy gap (0.75 eV) between T_1 and T_2, as well as tiny $\xi_{T1\rightarrow S0}$ (0.082 cm^{-1}) relative to $\xi_{T2\rightarrow S0}$ (0.318 cm^{-1}), the ISC process of $T_2 \rightarrow S_0$ is more competitive than $T_1 \rightarrow S_0$. Therefore, RTP of BTDA-H should come from ISC from $T_2 \rightarrow S_0$ rather than $T_1 \rightarrow S_0$. It is worth mentioning that the energy level corresponding to T_2 (2.81 eV) is close to the phosphorescence emission (480 nm) of BTDA-H in glass state solution (77 K). Of note, the energy differences (ΔE_{T1T2}) between T_1 states of hosts and T_2 state of BTDA-H are gradually increasing from TCN-H (0.00 eV), TCN-F (0.04 eV), TCN-Cl (0.35 eV) to TCN-Br (0.42 eV), which is consistent with the reduced I_{TADF}/I_{RTP} in sequence. According to the energy levels of four hosts and BTDA-H, it is easier for the energy transfer from T_2 of BTDA-H to T_1 of hosts rather than RISC. To further investigate effects of halogen atoms on TADF and RTP, 1 % TCN-H/BTDA-F, 1 % TCN-H/BTDA-Cl, and 1 % TCN-H/BTDA-Br were constructed by changing the guests and stabilizing the host. Compared with 1 % TCN-F/BTDA-F, 1 % TCN-Cl/BTDA-Cl, and 1 % TCN-Br/BTDA-Br, the new corresponding doping systems show longer afterglows, lasting for 9 s, 5 s and 1 s respectively (Fig. S3a). Based on previous literatures, constructing host–guest doping system requires consideration of compatibility, intermolecular interactions, and energy levels between host and guest [43,44]. Crystalline emission spectra show TCN-H and TCN-F have the same singlet state energy level (Fig. S40), while TCN-F, TCN-Cl and TCN-Br compared with TCN-H should have better compatibility with their corresponding BTDA luminogens due to more similar molecular structure. Therefore, the prolonged afterglows of new doping systems should be attributed to the reduced heavy-atom effect, as well as different intermolecular arrangement and stacking mode between TCN-H and the other hosts, better stabilizing the triplet excitons, which are confirmed by crystal analysis. To explore a time-saving and efficient method for lighting TADF and RTP, BTDA-Me was prepared based on similar molecular structure by a simple (Fig. 1a), gentle, and efficient synthesis method, and used as guest to build up a new doping system (1 % TCN-H/BTDA-Me) at doping ratio of 100:1 (Fig. 3f). Owing to the introduction of a methyl group, RTP emission maxima show bathochromic-shifts of 10 nm from 1 % TCN-H/BTDA-H to 1 % TCN-H/BTDA-Me, accompanied by the decreasing I_{TADF}/I_{RTP}. As expected, the new doping system, like 1 % TCN-H/BTDA-H, generates efficient RTP and TADF, with bright green afterglow lasting up to 6 s (Fig. 3f). Obviously, BTDA-Me provides a more time saving and active alternative for the impurities.

Polymethyl methacrylate (PMMA) can effectively suppress the non-radiative energy attenuation of the triplet exciton, boost large-scale fabrication of devices due to rigid environment, excellent flexibility, and transparency [45–48]. To further verify the adjustability of the intensity ratio between TADF and RTP, and explore the source of TADF emission, 1 % BTDA-H@PMMA, 1 % BTDA-F@PMMA, 1 % BTDA-Cl@PMMA, 1 % BTDA-Br@PMMA, and 1 % BTDA-Me@PMMA films were prepared by doping BTDA-H, BTDA-F, BTDA-Cl, BTDA-Br, and BTDA-Me into PMMA at doping concentration of 1:100 (Fig. 4a). Switching on/off a UV lamp of 365 nm (deoxygenation after irradiation of 60 s), 1 % BTDA-F@PMMA film presents the longest afterglow, lasting for 4 s, followed by 1 % BTDA-Cl@PMMA, 1 % BTDA-Me@PMMA, 1 % BTDA-H@PMMA and 1 % BTDA-Br@PMMA films, with TADF and RTP lifetimes of 126–315 ms and 102–341 ms separately. By comparison, the doping films show shorter TADF and RTP lifetimes than TCN-BTDA series, highlighting superiority of TCN-BTDA doping systems. When the temperature drops to 0 ^{O}C, afterglows of 1 % BTDA-F@PMMA, 1 % BTDA-Cl@PMMA, 1 % BTDA-Me@PMMA films prolong to more than 9 s, 7 s and 8 s in turn, indicating that PMMA films cannot effectively suppress molecular motion at RT (Fig. S46). Furthermore, RTP emission maxima of BTDA-H, BTDA-F, BTDA-Cl, and BTDA-Me shows blue shifts of 10 nm, 20 nm, 10 nm, and 15 nm in PMMA films compared with TCN series luminogens respectively, but with stable TADF emission maxima for BTDA-H and BTDA-F, as well as red shifts and blue shifts of 5 nm for BTDA-Cl and BTDA-Me in sequence. ΔE_{ST} of 1 % BTDA-H@PMMA, 1 % BTDA-F@PMMA, 1 % BTDA-Cl@PMMA, and 1 % BTDA-Me@PMMA films are 0.44 eV, 0.41 eV, 0.46 eV, and 0.50 eV, indicating slight decreases relative to that of TCN/BTDA systems. Based on the emission maxima, energy gaps (ΔE_{S1T2}) of BTDA-F, BTDA-Cl, and BTDA-Me are significantly reduced (Fig. S47), which should take responsible for the enhanced I_{TADF}/I_{RTP}. Notably, I_{TADF}/I_{RTP} of BTDA-Me, BTDA-F and BTDA-Cl are up to 0.8, 1.1, and 0.65 respectively. More interesting,

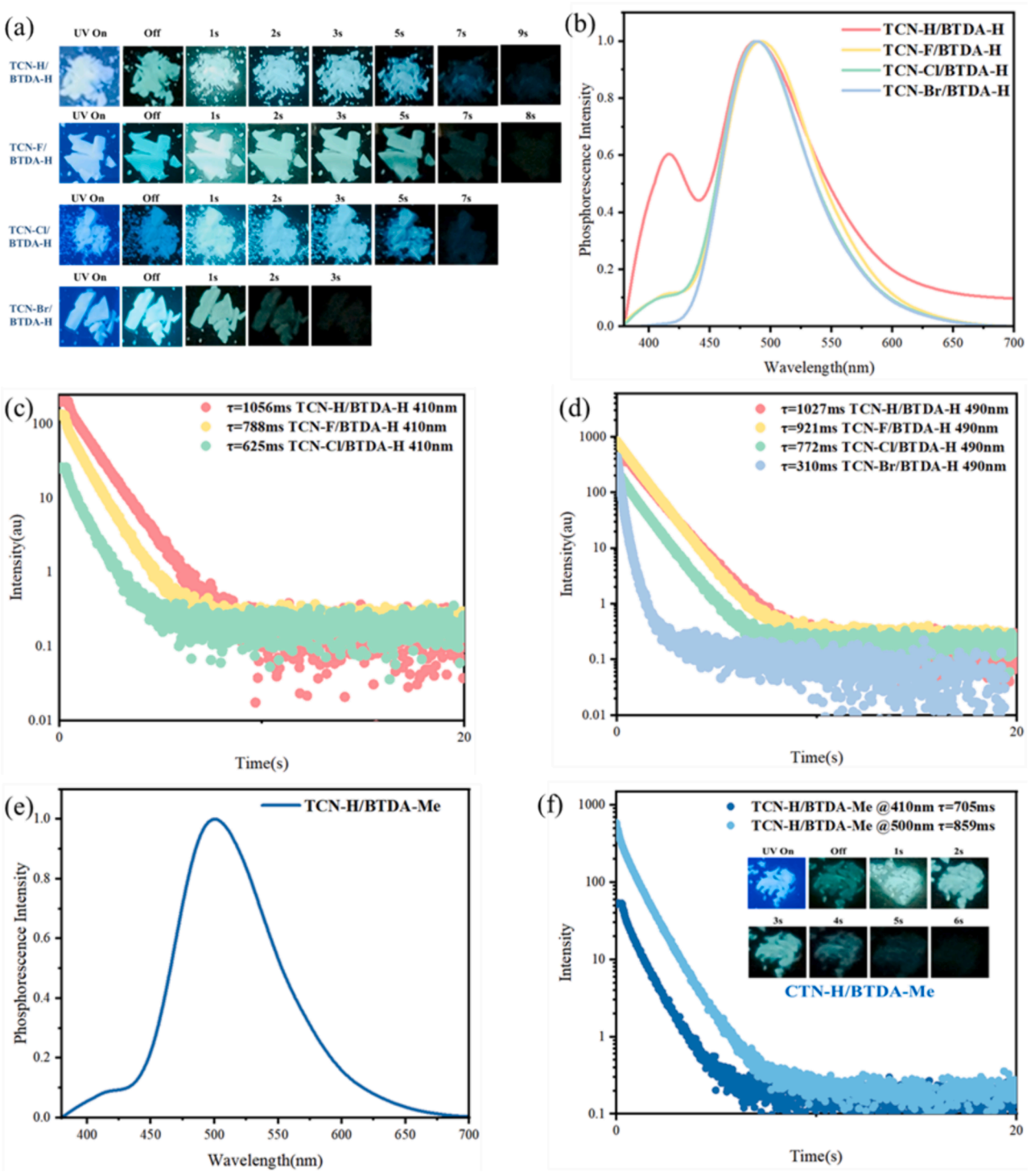

Fig. 3. (a) Digital photographs and (b) delay spectra of four doping systems with the same guest. (c) TADF and (d) RTP decay curves of 1 % TCN-H/BTDA-H, 1 % TCN-F/BTDA-H, 1 % TCN-Cl/BTDA-H and 1 % TCN-Br/BTDA-H (τ_d = 1 ms, λ_{ex}: 365 nm). (e) RTP decay spectra of 1 % TCN-H/BTDA-Me; (f) TADF and RTP decay curves of 1 % TCN-H/BTDA-Me (Inset: Digital photographs of 1 % TCN-H/BTDA-Me).

BTDA-H shows the reduced I_{TADF}/I_{RTP}, despite tiny decrease in ΔE_{S1T2}. As speculation, the PMMA matrix with carbonyl groups significantly enhances SOC of BTDA-H, leading to the reduced I_{TADF}/I_{RTP}, which is like the heavy atom effect mentioned above. By the on–off switching of 365 nm UV lamp, they show different afterglows. BTDA-H, BTDA-F and BTDA-Cl emit purple or blue fluorescence with emission maxima at 425 nm in PMMA films (Fig. 4c), while BTDA-Br generates near white fluorescence due to dual band emission with the same intensity, corresponding to fluorescence emission at 438 nm and phosphorescence emission at 507 nm respectively.

2.4. Stability bicomponent RTP system

Crystal engineering can stabilize triplet excitons and inhibit the diffusion of and oxygen, and thereby become the most important means to construct RTP materials [49–51]. Meanwhile, crystals have regular spatial arrangement and stacking modes, contributing to explore the underlying mechanisms behind phosphorescence by crystal analysis and

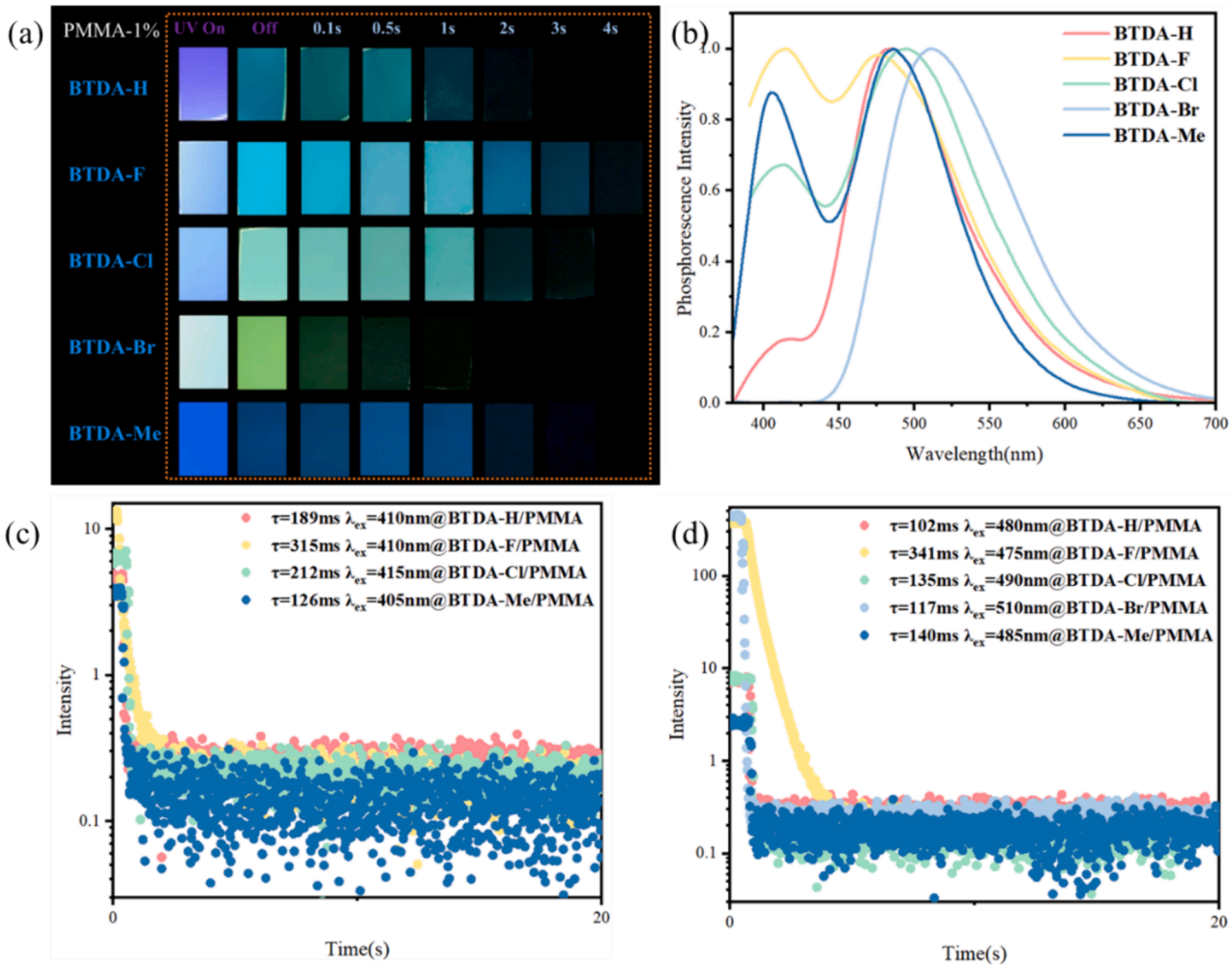

Fig. 4. (a) Digital photographs, (b) delay spectra, (c) TADF and (d) RTP decay curves of 1 % BTDA-H@PMMA, 1 % BTDA-F@PMMA, 1 % BTDA-Cl@PMMA, 1 % BTDA-Br@PMMA, and 1 % BTDA-Me@PMMA films (τ_d = 1 ms, λ_{ex}: 365 nm).

theoretical calculations. However, crystal engineering is often influenced by the environment, leading to poor repeatability, and resulting drastic fluctuations in phosphorescence performance. Fig. S35, shows that 1 % TCN-H/BTDA-H can emit ultralong phosphorescence within the large span adjustment range of doping ratio. What's more, the ultralong phosphorescence can be observed by rapid precipitation of the receiving liquid during the process of column chromatography and reduced pressure rotary evaporation (Fig. S42). More importantly, the above sample with long afterglow does not require prolonged exposure to ultraviolet light. The results indicate that 1 % TCN-H/BTDA-H doping system has high repeatability and stability in oxygen environments, which should be attributed to excellent crystallinity and compatibility of TCN and BTDA. In aqueous environments, intermolecular hydrogen bonds and interactions in host–guest doping systems are often destroyed, causing the disappearance or severe weakening of RTP. When four doping systems were soaked in water for more than one week, afterglow 1 % TCN-F/BTDA-F, 1 % TCN-Cl/BTDA-Cl and 1 % TCN-Br/BTDA-Br, can last for more than 7 s, 5 s and 3 s respectively (Fig.S43), only showing slight attenuation relative to anhydrous environment. More interesting, ground samples of four doping systems did not show an obvious reduction in afterglow lifetime, especially in the 1 % TCN-H/BTDA-H system. Compared with the initial sample, 1 % TCN-H/BTDA-H shows slightly extended afterglow lifetime and obviously increased I_{TADF}/I_{RTP} after grinding (Fig. 2a and Fig. 5a), leading to time-dependent afterglow from green to blue. The situation is rare due to grinding, which exposes the triplet excitons more to oxygen and destroys intermolecular interactions, often leading to phosphorescence quenching. To reveal the underlying mechanism, taking 1 % TCN-H/BTDA-H as an example, X-ray diffraction (XRD) of TCN, as well initial and ground 1 % TCN-H/BTDA-H samples were recorded. Fig. 5c shows that TCN-H displays a strong XRD signals at 24° before/after doping, indicating strong crystallizability. For 1 % TCN-H/BTDA-H system, grinding only leads to recession or disappear of a small amount of weak XRD signals, but main XRD signals remain stable. Obviously, the stable crystalline state and excellent compatibility make the RTP and TADF performance of 1 % TCN-H/BTDA-H basically unaffected by external mechanical forces. In addition, even if the 1 % TCN-H/BTDA-H sample is stored in the environment for one month, its phosphorescence activity also remains basically stability. By and large, the doping systems is insensitive to water, oxygen, and mechanical force.

2.5. *Mechanism of trace ingredient-mediated bicomponent RTP*

To reveal the intrinsic mechanism of trace ingredient-mediated bicomponent RTP systems, it is necessary to explore the intermolecular interactions and stacking modes of host and guest materials. Crystal analysis (Fig. S48-52) show TCN-H and TCN-F are monoclinic systems with a space group P 1 21/c 1, and a cell unit contains four molecules. In crystals (Fig. 6), two adjacent TCN-H molecules adopt antiparallel stacking patterns, and the centroid-to-centroid (C_g-C_g) and plane-to-plane (C_P-C_P) distances between two adjacent benzene rings are 4.064 Å and 3.637 Å respectively, corresponding a pitch angle of 63.5°, which

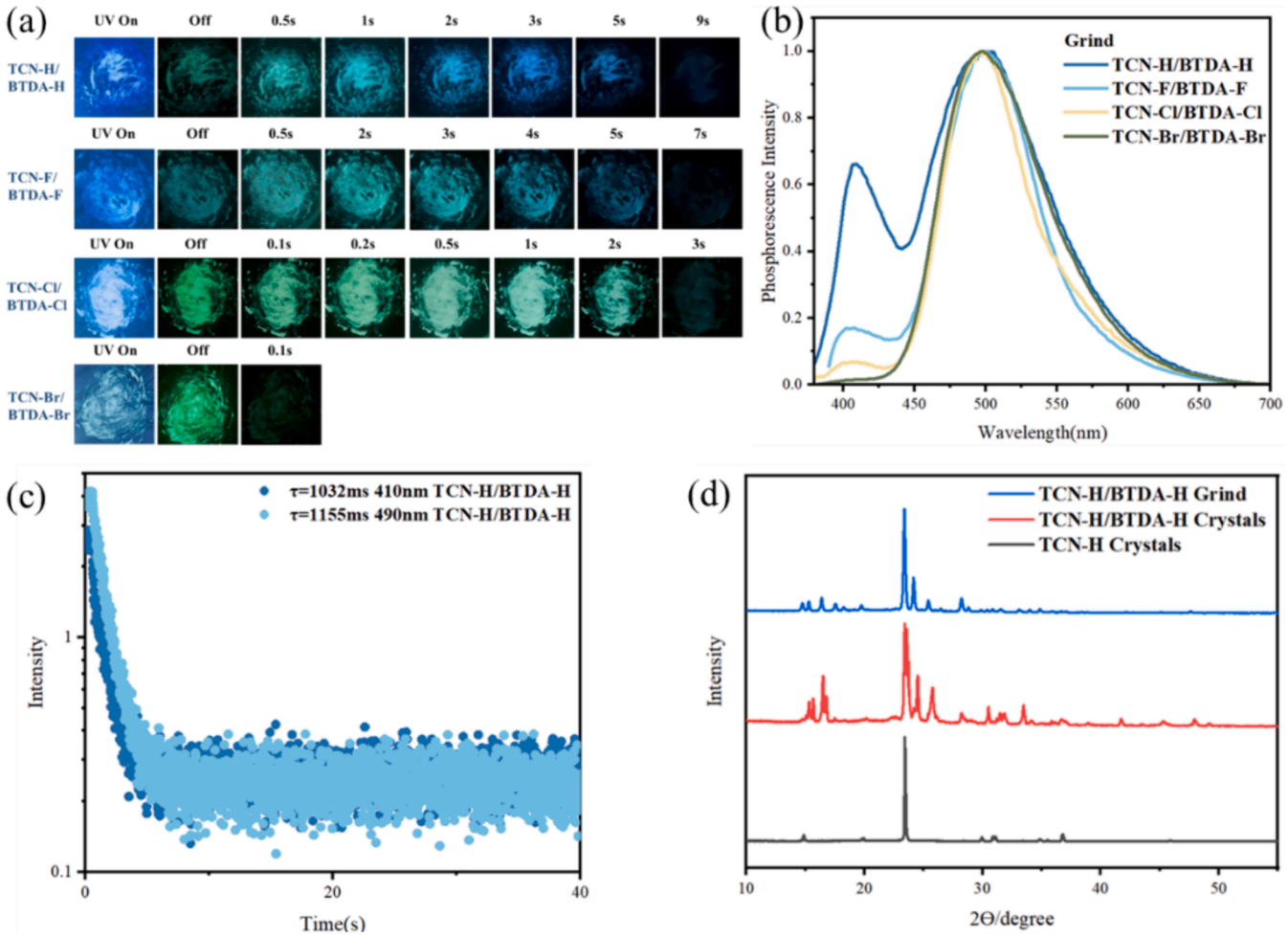

Fig. 5. (a) Digital photographs and (b) delay spectra of four doping systems after grinding (τ_d = 1 ms, λ_{ex}: 365 nm). (c) TADF and RTP decay curves of 1 % TCN-H/BTDA-H doping systems after grinding. (d) XRD patterns of crystal TCN-H, crystal, and ground 1 % TCN-H/BTDA-H samples.

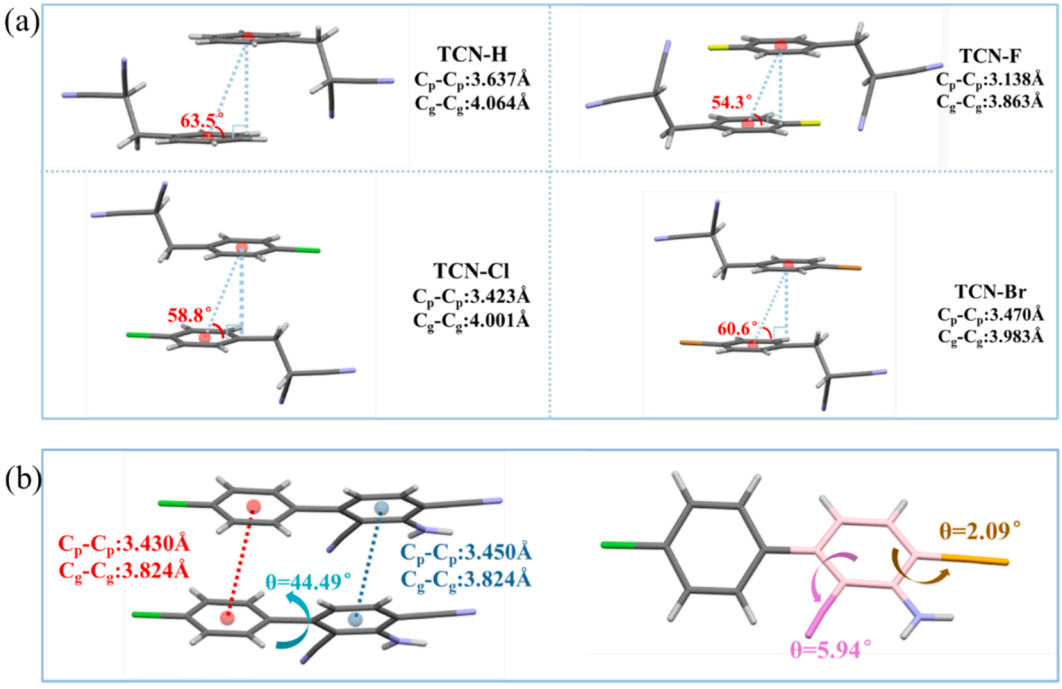

Fig. 6. The intermolecular stacking modes of (a) four hosts and (b) BTDA-Cl.

belongs to intermolecular H type stacking. Compared with TCN-H, the C_g-C_g and C_P-C_P distances between two adjacent benzene rings are shortened to 3.863 Å and 3.138 Å respectively in crystal TCN-F, corresponding a pitch angle of 54.3°, which belongs to intermolecular π-π stacking. TCN-Cl and TCN-Br also present monoclinic systems with a space group C 1 2/c 1, but a cell unit contains eight molecules. Between two adjacent molecules, intermolecular antiparallel stacking patterns can also be found in crystals TCN-Br and TCN-Cl. For TCN-Cl, the C_g-C_g and C_p-C_P distances are 4.001 Å and 3.423 Å respectively, corresponding a pitch angle of 58.8°. In crystal TCN-Br, the C_g-C_g and C_P-C_P distances between two adjacent benzene rings are 3.983 Å and 3.470 Å respectively, corresponding a pitch angle of 60.6° and intermolecular H type stacking. As reported in the literatures, intermolecular H type stacking can stable triple excitons [52–54], resulting in long phosphorescence lifetime for the doping systems. By comparison, TCN-F shows the strongest intermolecular π-π stacking, hydrogen bonds and weak interactions, whose one molecule forms twelve intermolecular hydrogen bonds with neighboring molecules, followed by TCN-Cl and TCN-Br, with ten intermolecular hydrogen bonds between one molecule and neighboring molecules. TCN-H has the the least intermolecular hydrogen bonds. Compared with PMMA, H type stacking and strong intermolecular π-π stacking of four hosts should play a more important role in prolonging RTP lifetimes of the doping systems. In a unit cell, four BTDA-Cl molecules are arranged like a windmill. Furthermore, BTDA-Cl shows twisted molecular configuration, with a dihedral angle of 44.49° between chlorobenzene unit and dicyanoaniline unit, but it presents face-to-face stacking mode along the a-axis direction, whose C_g-C_g and C_P-C_P distances between two adjacent chlorobenzene units are 3.824 Å and 3.450 Å respectively, as well C_g-C_g distance of 3.824 Å and C_P-C_P distance of 3.430 Å between two adjacent dicyanoaniline units, with a typical H stacking. Besides, two CN groups form dihedral angles of 5.94° and 2.09° with the benzene ring respectively, while NH_2 and the benzene ring are coplanar. For the single molecule, BTDA-Cl forms eleven intermolecular hydrogen bonds and weak interactions with its surrounding molecules (2.176, 2.376, 2.367, 2.889, 3.028 and 3.370 Å). Even so, BTDA-Cl still shows invisible afterglow at room temperature in crystalline state, which may be due to intermolecular parallel stacking reducing the dipole moment of the excited state, leading to slow ISC rate.

Combining X-ray single crystal diffraction data, the geometric configuration of four hosts and BTDA-H were optimized at the B3LYP/def2-SVP level using D4 dispersion correction. Then the highest occupied molecular orbitals (HOMO) and the lowest unoccupied molecular orbitals (LUMO) distribution, energy level, and ξ were obtained. With the introduction of halogen atoms and the increase of atomic number, HOMO energy level continuously increases, while LUMO energy level continues to decrease, resulting in a reduced optical bandgap, which is consistent with the redshifted fluorescence emission for TCN-Br and TCN-Cl than TCN-H and TCN-F (Fig. 7f and Fig. S40). HOMO and LUMO energy levels of BTDA-H embedded between HOMO and LUMO energy levels of four hosts, confirming that fluorescence emissions of 1 % TCN-H/BTDA-H, 1 % TCN-F/BTDA-H, 1 % TCN-Cl/BTDA-H and 1 % TCN-Br/BTDA-H come from BTDA-H. TCN-H gives tiny $\xi(S_1 \rightarrow T_3)$, $\xi(S_1 \rightarrow T_4)$ and $\xi(T_1 \rightarrow S_0)$, leading to ineffective ISC and phosphorescence radiation. $\xi(S_1 \rightarrow T_3)$ and ΔE_{S1T3} of TCN-F are 0.165 cm^{-1} and 0.49 eV in sequence, but its $\xi(T_1 \rightarrow S_0)$ is only 0.020 cm^{-1}, which is consistent with the absence of afterglow in the crystalline state. Compared with TCN-H, TCN-F has the enhanced ISC ability, but its T_1 is slightly lower than T_2 of BTDA-H, resulting in partial energy transfer between T_1 of TCN-F and T_2 of BTDA-H, which become ineffective phosphorescence radiation because of tiny $\xi(T_1 \rightarrow S_0)$ for TCN-F (0.020 cm^{-1}). The above tiny $\xi(T_1 \rightarrow S_0)$ combined with energy transfer should take the responsible for the reduced I_{TADF}/I_{RTP}, Φ_P and Φ_{TADF} for 1 % TCN-F/BTDA-H than 1 % TCN-H/BTDA-H. Different from TCN-H and TCN-F, phosphorescence radiation ability of TCN-Cl (0.368 cm^{-1}) and TCN-Br (3.653 cm^{-1}) is significantly enhanced due to large $\xi(T_1 \rightarrow S_0)$. Owing to equivalent $\xi(S_1 \rightarrow T_3)$ between TCN-Cl and TCN-F, as well as higher $\xi(T_1 \rightarrow S_0)$ for TCN-Cl than TCN-F, 1 % TCN-Cl/BTDA-H gives the shortened phosphorescence lifetime, increased Φ_P, and decreased I_{TADF}/I_{RTP}. TCN-Br has the strongest ISC and phosphorescence radiation ability in four hosts, whose $\xi(S_1 \rightarrow T_3)$ and $\xi(T_1 \rightarrow S_0)$ are 0.500 $cm^{-1}$and 3.653 cm^{-1} in turn, and energy transfer from T_2 of BTDA-H to T_1 of TCN-Br is feasible. Therefore, TCN-Br/BTDA-H has the highest Φ_P and the lowest I_{TADF}/I_{RTP} due to significantly increased ISC transitions and phosphorescence radiation. Besides, ΔE_{S1T2} between S_1 and T_1 states of BTDA-H is 0.54 eV based on theoretical calculation, which is close to 0.49 eV of 1 % TCN-H/BTDA-H and 0.44 eV of 1 % BTDA-H@PMMA, indicating that TADF of BTDA-H comes from the reversible intersystem crossing from T_2 to S_1.

2.6. Applications

In program display, different arrangement symbols have their own corresponding output results. As shown in Fig. 8a, different symbol sequences were designed and arranged by using long-lived 1 % TCN-H/

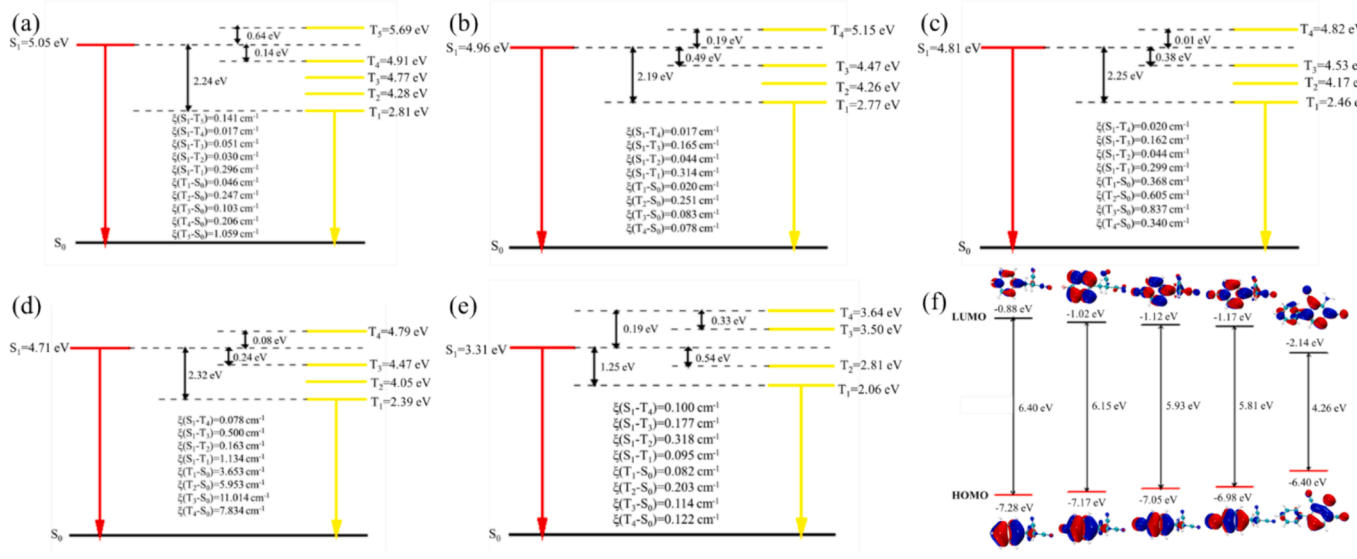

Fig. 7. Energy levels and spin orbit coupling constants (ξ) of (a) TCN-H, (b) TCN-F, (c) TCN-Cl, (d) TCN-Br, (e) BTDA-H; HOMO and LUMO distribution of four hosts and BTDA-Cl.

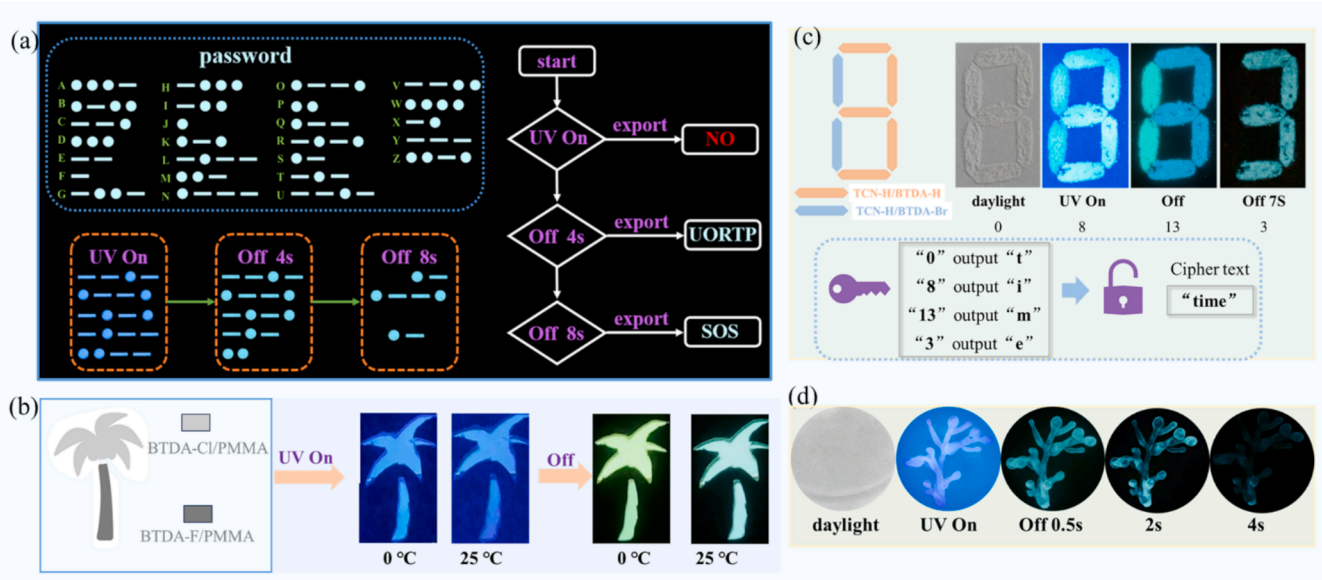

Fig. 8. (a) Program encryption by using 1% TCN-H/BTDA-H, 1% TCN-H/BTDA-F, and 1% TCN-H/BTDA-Br samples. (b) Data encryption by using 1% TCN-H/BTDA-H and 1% TCN-Br/BTDA-Br samples. (c) A "tree" pattern drawn directly on the common filter paper by using 1% TCN-H/BTDA-H samples. (d) A "tree" pattern constructed by 1% BTDA-F@PMMA and 1% BTDA-Cl@PMMA films with various fluorescence and afterglow at different temperatures.

BTDA-H, 1 % TCN-H/BTDA-F, and 1 % TCN-H/BTDA-Br samples. However, the input information sequences are unable to retrieve and read under 365 nm UV irradiation due to the absence of password in the fifth line. After turning off 365 nm UV lamp for 4 s, the symbols arranged with 1 % TCN-H/BTDA-Br disappear. By comparing the visible arrangement symbols with the password book, the output information can be retrieved and read as "UORTP". When the time extends to 8 s, the arrangement symbols continue to change as the symbols coming from 1 % TCN-H/BTDA-F samples fade away. At this time, the output information is recognized as "SOS". Thereby, different information can be obtained over time, which has promising application prospects in anti-counterfeiting and confidentiality. 1 % TCN-H/BTDA-H and 1 % TCN-Br/BTDA-Br exhibit similar fluorescence emission and high-contrast afterglow color and lifetime, which make them very suitable for data encryption. Subsequently, number 8 was outlined by 1 % TCN-H/BTDA-H and 1 % TCN-Br/BTDA-Br doping systems. Owing to absorption spectra of two doping systems concentrated on UV band below 400 nm, only the trace of writing "8″ could be found under natural light, corresponding to number "0". Under 365 nm UV irradiation, bright blue number "8" was clearly visible, which transformed into number "13" after turning off UV lamp due to similar fluorescence emission and distinct afterglow colors between 1 % TCN-H/BTDA-H and 1 % TCN-H/BTDA-Br doped systems. When the UV lamp had been turned off for 3 s, only number "3" draw by 1 % TCN-H/BTDA-H could be observed, while number "1" draw by 1 % TCN-H/BTDA-Br had completely disappeared, which were due to 1 % TCN-H/BTDA-H with longer RTP lifetimes compared with 1 % TCN-H/BTDA-Br. Setting the numbers "0", "8", "13" and "3" to t, i, m, and e in turn, the encrypted information can be interpreted as "time" by switching on–off UV lamp. Based on long-lived RTP and TADF characteristics of 1 % TCN-H/BTDA-H, a tree was directly drawn on a piece of common filter paper by using DCM solution (1×10^{-4} M) of 1 % TCN-H/BTDA-H. After solvent evaporation, the "tree" is invisible in sunlight. Switching on 365 nm UV lamp, a blue purple "tree" is clearly visible, which turns into blue "tree" after turning off the UV lamp, lasting for 4 s. Based on the reverse temperature responses between TADF and RTP, a "coconut tree" was constructed by choosing BTDA-F and BTDA-Cl doped PMMA films. Under 365 nm UV radiation, the color change of "coconut tree" is not significant when temperature increases to 25 ^{O}C from 0 ^{O}C. Switching off the 365 nm UV lamp, the "coconut tree" presents yellowish green at 0 ^{O}C, which becomes blue green at 25 ^{O}C, indicating a significant vision change.

3. Conclusions

By one pot multi-step reactions, a series of TCN luminogens and novel BTDA derivatives were prepared and found, whose structures were characterized and confirmed by NMR, HR-MS, and single-crystal X-ray diffraction. TCN luminogens show excitation dependent dual band fluorescence emission in DCM solution, while BTDA derivatives have dual-state fluorescence emission or AIEE activity in THF-H_2O solution. The TCN luminogens containing trace BTDA derivatives firstly achieved four bicomponent host–guest doping systems, with green afterglows of 1.5–3.5 s. By melting and optimizing bicomponent doping ratio, 1 % TCN-H/BTDA-H presents persistent dual-band ultralong afterglows at 410 nm and 490 nm, corresponding to TADF and RTP respectively, whose delay lifetimes are up to 1056 ms and 1027 ms in sequence. The low-temperature phosphorescence, construction of multiple bicomponent systems, and theoretical calculation illustrated the TADF and RTP of the bicomponent systems come from BTDA derivatives rather than TCN luminogens. Crystal and XRD analyses showed that H type stacking and excellent crystallinity took responsible for long lifetime of 1 % TCN-H/BTDA-H, as well as water and oxygen resistance stability of TADF and RTP. The relative intensity between TADF and RTP is mainly affected by energy differences between T_1 of host and T_2 of guest, and $\xi(T_1 \rightarrow S_0)$ of host, which can be well adjusted by grinding, temperature, host, and guest materials, achieving color-tunable and time-dependent afterglow. Besides, the unusual doping systems with long-lived TADF and RTP were easily expanded based on the similar molecular structure and efficient synthesis method. Finally, the high-level digital and program encryption, and anti-counterfeiting patterns were successfully constructed based on temperature sensitivity, and different TADF and RTP afterglow lifetimes of the doping systems. This work will provide a novel understanding of dual band and long-lived TADF and RTP and contribute to boost the development of dynamic anti-counterfeiting and information encryption.

CRediT authorship contribution statement

Lijuan Shi: Writing – original draft, Visualization, Validation, Methodology, Investigation, Formal analysis, Data curation,

Conceptualization. **Jiaqi Liu:** Software. **Lei Ma:** Software. **Yongtao Wang:** Writing – review & editing, Validation, Supervision, Resources, Project administration, Methodology, Funding acquisition, Formal analysis, Data curation, Conceptualization.

Declaration of competing interest

The authors declare that they have no known competing financial interests or personal relationships that could have appeared to influence the work reported in this paper.

Data availability

No data was used for the research described in the article.

Acknowledgment

This work was supported by the Guangxi Natural Science Foundation (Grant No. 2024GXNSFAA010423 and 2020GXNSFAA159147) and the National Natural Science Foundation of China (Grant No. 21766030 and 21566034).

Appendix A. Supplementary data

Supplementary data to this article can be found online at https://doi.org/10.1016/j.cej.2024.152492.

References

[1] S. Xu, R. Chen, C. Zheng, W. Huang, Excited state modulation for organic afterglow: Materials and applications, Adv. Mater. 28 (2016) 9920–9940.
[2] Z. Wu, H. Choi, Z.M. Hudson, Achieving white-light emission using organic persistent room temperature phosphorescence, Angew. Chem. Int. Ed. 62 (2023) 01186.
[3] Z. Yang, Z. Mao, X. Zhang, D. Ou, Y. Mu, Y. Zhang, C. Zhao, S. Liu, Z. Chi, J. Xu, Y. C. Wu, P.Y. Lu, A. Lien, M.R. Bryce, Intermolecular electronic coupling of organic units for efficient persistent room-temperature phosphorescence, Angew. Chem. Int. Ed. 128 (2016) 2221–2225.
[4] A. Köhler, H. Bässler, Triplet states in organic semiconductors, Mater. Sci. Eng. r. 66 (2009) 71–109.
[5] J. Shi, W. Tao, Y. Zhou, G. Liang, Efficient room-temperature phosphorescence with tunable lifetime through light modulation from flexible polymer films, Chem. Eng. J. 475 (2023) 146178.
[6] H. Ju, H. Zhang, L.X. Hou, M. Zuo, M. Du, F. Huang, Q. Zheng, Z.L. Wu, Polymerization-induced crystallization of dopant molecules: An efficient strategy for room-temperature phosphorescence of hydrogels, J. Am. Chem. Soc. 145 (2023) 3763–3773.
[7] X. Chen, W. Dai, X. Wu, H. Su, C. Chao, Y. Lei, J. Shi, B. Tong, Z. Cai, Y. Dong, Fluorene-based host-guest phosphorescence materials for information encryption, Chem. Eng. J. 426 (2021) 131607.
[8] Y. Lei, W. Dai, J. Guan, S. Guo, F. Ren, Y. Zhou, J. Shi, B. Tong, Z. Cai, J. Zheng, Y. Dong, Wide-range color-tunable organic phosphorescence materials for printable and writable security inks, Angew. Chem. Int. Ed. 59 (2020) 16054–16060.
[9] Y. Sun, S. Liu, L. Sun, S. Wu, G. Hu, X. Pang, A.T. Smith, C. Hu, S. Zeng, W. Wang, Y. Liu, M. Zheng, Ultralong lifetime and efficient room temperature phosphorescent carbon dots through multi-confinement structure design, Nat. Commun. 11 (2020) 5591.
[10] H. Uoyama, K. Goushi, K. Shizu, H. Nomura, C. Adachi, Highly efficient organic light-emitting diodes from delayed fluorescence, Nature. 492 (2012) 234–238.
[11] G. Zhan, Z. Liu, Z. Bian, C. Huang, Recent advances in organic light-emitting diodes based on pure organic room temperature phosphorescence materials, Front. Chem. 7 (2019) 305.
[12] S.M.A. Fateminia, Z. Mao, S. Xu, Z. Yang, Z. Chi, B. Liu, Organic nanocrystals with bright red persistent room-temperature phosphorescence for biological applications, Angew. Chem. Int. Ed. 56 (2017) 12160–12164.
[13] J. Zhi, Q. Zhou, H. Shi, Z. An, W. Huang, Organic room temperature phosphorescence materials for biomedical applications, Chem. Asian J. 15 (2020) 947–957.
[14] T. Zhang, H. Gao, A. Lv, Z. Wang, Y. Gong, D. Ding, H. Ma, Y. Zhang, W.Z. Yuan, Hydrogen bonding boosted the persistent room temperature phosphorescence of pure organic compounds for multiple applications, J. Mater. Chem. C 7 (2019) 9095–9101.
[15] X. Yan, H. Peng, Y. Xiang, J. Wang, L. Yu, Y. Tao, H. Li, W. Huang, R. Chen, Recent advances on host–guest material systems toward organic room temperature phosphorescence, Small. 18 (2021) 2104073.
[16] M. Li, X. Cai, Z. Chen, K. Liu, W. Qiu, W. Xie, L. Wang, S.-J. Su, Boosting purely organic room-temperature phosphorescence performance through a host–guest strategy, Chem. Sci. 12 (2021) 13580–13587.
[17] J. Yang, X. Wu, J. Shi, B. Tong, Y. Lei, Z. Cai, Y. Dong, Achieving efficient phosphorescence and mechanoluminescence in organic host–guest system by energy transfer, Adv. Funct. Mater. 31 (2021) 08072.
[18] J. Wei, B. Liang, R. Duan, Z. Cheng, C. Li, T. Zhou, Y. Yi, Y. Wang, Induction of strong long-lived room-temperature phosphorescence of n-phenyl-2-naphthylamine molecules by confinement in a crystalline dibromobiphenyl matrix, Angew. Chem. Int. Ed. 55 (2016) 15589–15593.
[19] Q. Gao, M. Shi, M. Chen, X. Hao, G. Chen, J. Bian, B. Lü, J. Ren, F. Peng, Facile preparation of full-color tunable room temperature phosphorescence cellulose via click chemistry, Small 20 (2024) 2309131.
[20] J. Yuan, Z. Li, J. Chen, Y. Qi, P. Li, T. Yu, Y. Tao, R. Chen, Boosting organic room-temperature phosphorescence performance through joint luminescence sensitization, J. Mater. Chem. C 11 (2023) 113.
[21] L. Gao, J. Huang, L. Qu, X. Chen, Y. Zhu, C. Li, Q. Tian, Y. Zhao, C. Yang, Stepwise taming of triplet excitons via multiple confinements in intrinsic polymers for long-lived room-temperature phosphorescence, Nat. Commun. 14 (2023) 7252.
[22] Y. Sun, J. Liu, X. Pang, X. Zhang, J. Zhuang, H. Zhang, C. Hu, M. Zheng, B. Lei, Y. Liu, Temperature-responsive conversion of thermally activated delayed fluorescence and room-temperature phosphorescence of carbon dots in silica, J. Mater. Chem. C 8 (2020) 5744–5751.
[23] J. Han, W. Feng, D.Y. Muleta, C.N. Bridgmohan, Y. Dang, G. Xie, H. Zhang, X. Zhou, W. Li, L. Wang, D. Liu, Y. Dang, T. Wang, W. Hu, Small-molecule-doped organic crystals with long-persistent luminescence, Adv. Funct. Mater. 29 (2019) 02503.
[24] J. Li, X. Li, G. Wang, X. Wang, M. Wu, J. Liu, K. Zhang, A direct observation of up-converted room-temperature phosphorescence in an anti-kasha dopant-matrix system, Nat. Commun. 14 (2023) 1987.
[25] Y. Zhou, L. Jin, J. Chen, W. Hong, G. Liang, W. Qin, Five-in-one: Dual-mode ultralong persistent luminescence with multiple responses from amorphous polymer films, Chem. Eng. J. 463 (2023) 142506.
[26] J. Jovaišaitė, S. Kirschner, S. Raišys, G. Kreiza, P. Baronas, S. Juršėnas, M. Wagner, Diboraanthracene-doped polymer systems for colour-tuneable room-temperature organic afterglow, Angew. Chem. Int. Ed. 62 (2022) 15071.
[27] J. Hu, M. Lei, L. Yan, L. Chen, Y. Yang, J. Zheng, X. Liu, B. Xu, Carbon dot-based afterglow composite with tunable room temperature phosphorescence and thermally activated delayed fluorescence and their anti-counterfeiting and encryption application, Chem. Eng. J. 489 (2024) 151245.
[28] M. Park, H.S. Kim, H. Yoon, J. Kim, S. Lee, S. Yoo, S. Jeon, Controllable singlet–triplet energy splitting of graphene quantum dots through oxidation: From phosphorescence to tadf, Adv. Mater. 32 (2020) 2000936.
[29] L. Ai, W. Xiang, J. Xiao, H. Liu, J. Yu, L. Zhang, X. Wu, X. Qu, S. Lu, Tailored fabrication of full-color ultrastable room-temperature phosphorescence carbon dots composites with unexpected thermally activated delayed fluorescence, Adv. Mater. (2024) 2401220.
[30] Z. Xiao, N. Li, W. Yang, Z. Huang, X. Cao, T. Huang, Z. Chen, C. Yang, Saccharin-derived multifunctional emitters featuring concurrently room temperature phosphorescence, thermally activated delayed fluorescence and aggregation-induced enhanced emission, Chem. Eng. J. 419 (2021) 129628.
[31] C. Chen, Z. Chi, K.C. Chong, A.S. Batsanov, Z. Yang, Z. Mao, Z. Yang, B. Liu, Carbazole isomers induce ultralong organic phosphorescence, Nat. Mater. 20 (2020) 175–180.
[32] X. Zhang, C. Qian, Z. Ma, X. Fu, Z. Li, H. Jin, M. Chen, Z. Ma, Selective expression of organic p hosphorescence units: When h-benzo[f]indole meets 7h-benzo[c] carbazole, Chem. Mat. 35 (2023) 2624–2634.
[33] C. Qian, Z. Ma, X. Fu, X. Zhang, Z. Li, H. Jin, M. Chen, H. Jiang, X. Jia, Z. Ma, More than carbazole derivatives activate room temperature ultralong organic phosphorescence of benzoindole derivatives, Adv. Mater. 34 (2022) 220544.
[34] N. Campbell, B.M. Barclay, Recent advances in the chemistry of carbazole, Chem. Rev. 40 (1947) 359–380.
[35] H. Xiao, D.S. Zheng, L.Y. Zhang, L.J. Xu, Z.N. Chen, Ultra-long room temperature phosphorescence with the efficiency over 64% induced by 1% impurity doping, Adv. Funct. Mater. 33 (2023) 14241.
[36] Bingbing Ding, L.M., Zizhao Huang, Xiang Ma*, He Tian, Engendering persistent organic room temperature phosphorescence by trace ingredient incorporation, Sci. Adv. 19 (2021) eabf9668.
[37] W. Qiao, M. Yao, J. Xu, H. Peng, J. Xia, X. Xie, Z.A. Li, Naphthyl substituted impurities induce efficient room temperature phosphorescence, Angew. Chem. Int. Ed. 10 (2023) 15911.
[38] C. Qian, Z. Ma, B. Yang, X. Li, J. Sun, Z. Li, H. Jiang, M. Chen, X. Jia, Z. Ma, Carbazole&benzoindole-based purely organic phosphors: A comprehensive phosphorescence mechanism, tunable lifetime and an advanced encryption system, J. Mater. Chem. C 9 (2021) 14294–14302.
[39] H. Jin, X. Zhang, Z. Ma, C. Qian, X. Fu, Z. Li, M. Chen, Y. Guan, Z. Ma, Photo-activated time-dependent color-changeable ultralong organic room temperature phosphorescence by co-doping strategy, J. Mater. Chem. C 11 (2023) 11571–11579.
[40] X. Xu, Z. Chen, Y. Lei, X. Sun, M. Liu, H. Wu, X. Huang, Guest-activated quaternary ammonium salt hosts emit room temperature phosphorescence, Chem. Commun. 58 (2022) 11143–11146.
[41] X. Zheng, J. Jiang, Q. Lin, C. Li, J. Chen, S. Wang, Q. Han, X. Ye, Y. Liu, X. Tao, Excitation- & concentration-dependent color-tunable ultra-long phosphorescence of isophthalonitriles doped polymers, Chem. Eng. J. 469 (2023) 143929.

[42] Z. Lin, R. Kabe, N. Nishimura, K. Jinnai, C. Adachi, Organic long-persistent luminescence from a flexible and transparent doped polymer, Adv. Mater. 30 (2018) 1803713.
[43] Y. Wang, J. Yang, M. Fang, Y. Yu, B. Zou, L. Wang, Y. Tian, J. Cheng, B.Z. Tang, Z. Li, Förster resonance energy transfer: An efficient way to develop stimulus-responsive room-temperature phosphorescence materials and their applications, Matter 3 (2020) 449–463.
[44] Y. Zhang, S. Zhang, G. Liu, Q. Sun, S. Xue, W. Yang, Rational molecular and doping strategies to obtain organic polymers with ultralong rtp, Chem. Sci. 14 (2023) 5177–5181.
[45] S. Xiong, Y. Xiong, D. Wang, Y. Pan, K. Chen, Z. Zhao, D. Wang, B.Z. Tang, Achieving tunable organic afterglow and uv-irradiation-responsive ultralong room-temperature phosphorescence from pyridine-substituted triphenylamine derivatives, Adv. Mater. 35 (2023) 2301874.
[46] S. Yuan, Y. Zhang, J. Chen, Y. Yu, L. Yue, Q. Sun, H. Zhang, S. Xue, W. Yang, Effectively unlocking the potential molecular room temperature phosphorescence of pure carbazole derivatives, Adv. Opt. Mater. 10 (2022) 2200090.
[47] J. Chen, Y. Zhang, S. Zhang, G. Liu, Q. Sun, S. Xue, W. Yang, Two-phase rubber–plastic matrices' stabilization of organic room-temperature phosphorescence afterglows better than plastic matrix, Small Structures 4 (2023) 00101.
[48] C. Wang, Y. Zhang, Z. Wang, Y. Zheng, X. Zheng, L. Gao, Q. Zhou, J. Hao, B. Pi, Q. Li, C. Yang, Y. Li, K. Wang, Y. Zhao, Photo-induced dynamic room temperature phosphorescence based on triphenyl phosphonium containing polymers, Adv. Funct. Mater. 32 (2022) 2111941–2111951.
[49] J. Jin, H. Jiang, Q. Yang, L. Tang, Y. Tao, Y. Li, R. Chen, C. Zheng, Q. Fan, K. Y. Zhang, Q. Zhao, W. Huang, Thermally activated triplet exciton release for highly efficient tri-mode organic afterglow, Nat. Commun. 11 (2020) 842.
[50] M. Singh, K. Liu, S. Qu, H. Ma, H. Shi, Z. An, W. Huang, Recent advances of cocrystals with room temperature phosphorescence, Adv. Opt. Mater. 9 (2021) 2002197.
[51] F. Nie, B. Zhou, D. Yan, Ultralong room temperature phosphorescence and reversible mechanochromic luminescence in ionic crystals with structural isomerism, Chem. Eng. J. 453 (2023) 139806.
[52] S. Cai, H. Shi, J. Li, L. Gu, Y. Ni, Z. Cheng, S. Wang, W.W. Xiong, L. Li, Z. An, W. Huang, Visible-light-excited ultralong organic phosphorescence by manipulating intermolecular interactions, Adv. Mater. 29 (2017) 1701244.
[53] S. Li, L. Fu, X. Xiao, H. Geng, Q. Liao, Y. Liao, H. Fu, Regulation of thermally activated delayed fluorescence to room-temperature phosphorescent emission channels by controlling the excited-states dynamics via J- and H-aggregation, Angew. Chem. Int. Ed. 60 (2021) 18059–18064.
[54] L. Tu, Y. Fan, C. Bi, L. Xiao, Y. Li, A. Li, W. Che, Y. Xie, Y. Zhang, S. Xu, W. Xu, Q. Li, Z. Li, How temperature and hydrostatic pressure impact organic room temperature phosphorescence from h-aggregation of planar triarylboranes and the application in bioimaging, Sci. China-Chem. 66 (2023) 816–825.